Analysis of Single-Event Transients (SETs) Using Machine Learning (ML) and Ionizing Radiation Effects Spectroscopy (IRES)

T. D. Loveless, *Senior Member, IEEE*, D. R. Reising, *Senior Member, IEEE*, J. C. Cancelleri, L. W. Massengill, *Fellow, IEEE*, and D. McMorrow, *Fellow, IEEE*

***Abstract*— A methodology for automating the identification of single-event transients (SETs) through ionizing radiation effects spectroscopy (IRES) and machine learning (ML) is provided. IRES enhances the identification of SETs through statistical analysis of waveform behavior, allowing for the capture of subtle circuit dynamics changes. Automated identification of SETs is facilitated by a *k*-nearest neighbors (*k*NNs) ML algorithm with IRES data. One-hundred thousand waveforms were measured from CMOS phase-locked loop (PLL) circuits irradiated at the Naval Research Laboratory's two-photon absorption (TPA) laser facility. Known SET signatures were used to train various *k*NN models based on statistical features derived from several standard circuit metrics and eight moment-generating functions. Results show that SETs can be automatically identified by the *k*NN models, with several features resulting in greater than 98% correct identification of SETs. The tradeoffs in ML-based anomaly detection, based on the size of available training sets, choice in signal metric, and the number of included statistical moment-generating functions are discussed, along with opportunities for the future development of specific event-type classification, *in situ* measurement, and real-time classification of data.**

***Index Terms*— Ionizing radiation effects spectroscopy (IRES), *k*-nearest neighbors (*k*NNs), machine learning (ML), phase-locked loops (PLLs), radiation effects, single-event effects (SEEs), single-event transients (SETs), spectroscopy, time frequency analysis, two photon absorption (TPA).**

I. Introduction

THIS article documents the first use of machine learning (ML) to automatically identify and classify single-event effects (SEEs). SEEs are pervasive in modern spacecraft electronics systems; ionizing radiation is present in the external environment and emanates from processing and packaging material integral to a circuit. Aggressive integrated circuit (IC) density and power scaling have propelled this issue to the forefront of reliability concerns. SEEs can be further exacerbated in analog, mixed-signal, and system-on-chip (SoC) applications that are often challenging to interrogate [1]–[5]. In analog, mixed-signal, and SoC components, the effect of a single-event particle strike is the generation of a transient signal (single-event transient or SET) that interacts with the legitimate signals propagating through a circuit or perturbs the functionality of the circuit. Here, a method of detecting and classifying SETs in arbitrarily complex devices and ICs using ionizing radiation effects spectroscopy (IRES) [6], [7] and ML is discussed. SET vulnerable circuit nodes in a CMOS phase-locked loop (PLL) circuit are identified through time-frequency analysis of output signatures. One-hundred thousand waveforms were measured at the Naval Research Laboratory's two-photon absorption (TPA) laser facility, and ML via a *k*-nearest neighbors (*k*NNs) algorithm was used to classify nominal data and transient data based on statistical features. The statistical features, derived from several standard circuit metrics and up to eight moment-generating functions, show that SETs can be automatically identified by the *k*NN models, with several features resulting in greater than 98% correct identification of SETs. The findings presented herein offer the possibility of on-board and *in situ* event detection and diagnosis through the embedded computational capabilities offered through SoCs. Tradeoffs in the signal metrics, dimension, and the number of required training samples are discussed.

Manuscript received November 13, 2020; revised January 1, 2021; accepted January 7, 2021. Date of publication January 11, 2021; date of current version August 16, 2021. This work was supported in part by the Department of the Navy, Office of Naval Research under ONR award number N00164-19-1-1004 and the Defense Threat Reduction Agency under award number HDTRA1-17-1-0003.

T. D. Loveless and D. R. Reising are with the Electrical Engineering Department, University of Tennessee at Chattanooga, Chattanooga, TN 37403 USA (e-mail: daniel-loveless@utc.edu).

J. C. Cancelleri was with the Electrical Engineering Department, University of Tennessee at Chattanooga, Chattanooga, TN 37403 USA. He is now with NASA MSFC, Huntsville, AL 35808 USA (e-mail: joseph.c.cancelleri@nasa.gov).

L. W. Massengill is with the Department of Electrical Engineering and Computer Science, Vanderbilt University, Nashville, TN 37235 USA (e-mail: lloyd.massengill@vanderbilt.edu).

D. McMorrow is with the Naval Research Laboratory, Washington, DC 20375 USA (e-mail: dale.mcmorrow@nrl.navy.mil).

Color versions of one or more figures in this article are available at https://doi.org/10.1109/TNS.2021.3050879.

Digital Object Identifier 10.1109/TNS.2021.3050879

II. Background

A. Ionizing Radiation Effects Spectroscopy

Degradation of performance and loss of information are some of the biggest concerns caused by ionizing radiation. Mitigation of radiation effects often involves equipping circuits with larger capacitors, increased form factors, and increased current drives, all of which may reduce the severity of SETs. The drawback of these brute-force preventative measures is that they require adverse tradeoffs in area, power, and bandwidth, and diminishing the severity of these effects requires prior knowledge of where a particular circuit is susceptible.

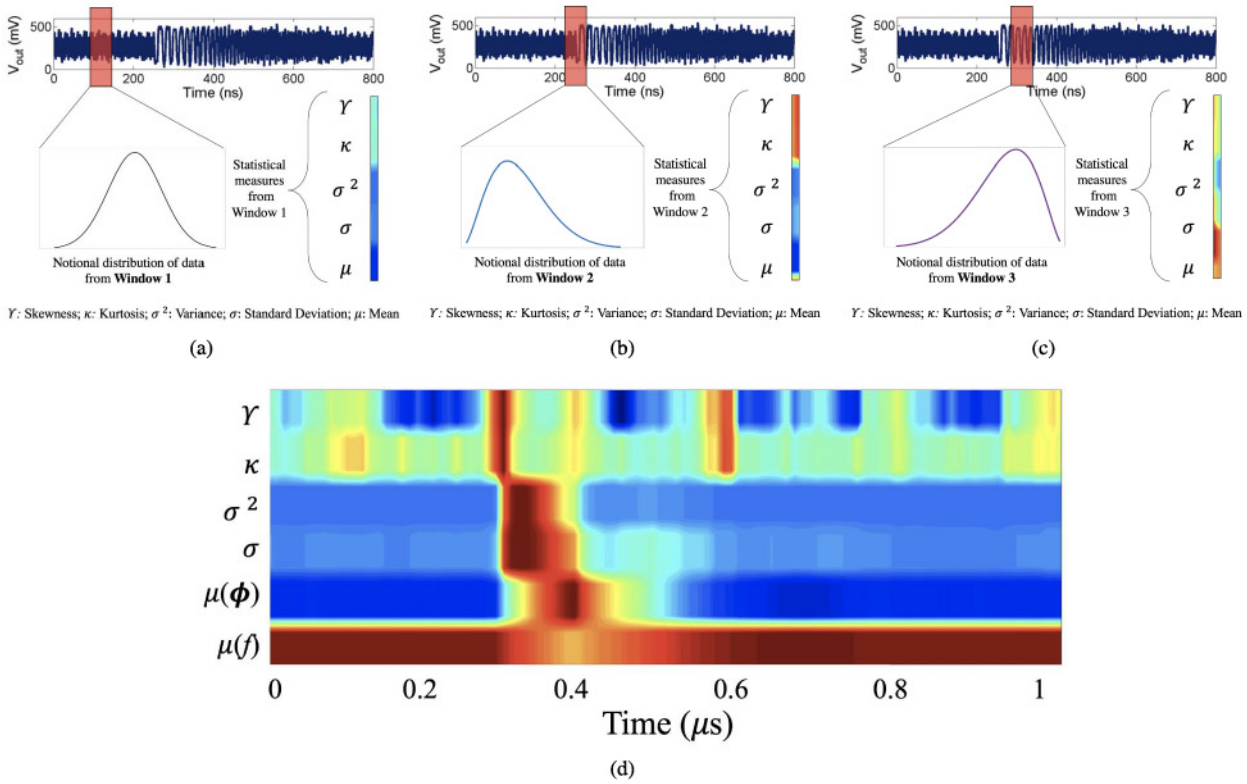

Fig. 1. Example IRES spectrogram (d) showing the skewness (γ), kurtosis (κ), variance (σ^2), standard deviation (σ), and mean (μ) of the PLL's output phase (ϕ), as well as the μ of the PLL's output frequency (f) obtained via time-frequency analysis of the output waveform. The IRES spectrogram was obtained through a sliding-window analysis as shown in (a)–(c); in this case, the frequency spectra were obtained within each window and Gaussian window filters were employed as in [7]. The sliding windows were sized to contain 20% of the total number of recorded time steps and shifted by a value of 1, corresponding to a 95% overlap. The relevant statistical measures within each window were recorded and visualized in a time sequence. Each timestamp corresponds to the starting time of the sliding window. The color bars represent the normalized values of the statistical measures (ranging from 0 (blue or light color) to 1 (red or dark color).

On the other hand, targeted radiation-hardening-by-design (RHBD) to improve performance while minimizing tradeoffs is costly and not feasible for many systems. IRES allows for a system-level analysis of radiation effects, which may reduce such brute-force RHBD by improving the understanding of the device and circuit degradation on the system while maintaining the ability to identify specific failure points. In this work, IRES is coupled with ML to identify and classify transient signatures *in situ*.

IRES is a technique derived from radio frequency-distinct native attributes (RF-DNA) fingerprinting, a signal-processing technique often found in wireless communications applications that exploits statistical features from waveforms associated with circuits or systems [8]–[19]. The detailed process for obtaining IRES spectrograms from a transient source is described in [7]. In this work, IRES is used to analyze a 130-nm CMOS PLL circuit, a core component in SoC applications. However, IRES can be used to analyze any arbitrarily complex waveform, as it does not depend on the thresholding of a performance metric and can be applied to static and dynamic waveforms alike through the sliding statistical analysis [7].

Fig. 1 shows an example IRES spectrogram generated via time-frequency analysis of a PLL's output waveform. In this case, the cycle-to-mean phase jitter and instantaneous frequency in the output waveform is visualized in the IRES spectrogram and includes the mean (μ), standard deviation (σ), variance (σ^2), kurtosis (κ), and skewness (γ) statistical measures. IRES spectrograms are generally obtained through a sliding-window analysis. Here, the frequency spectra were obtained within each window, and Gaussian window filters were employed as in [7]. The sliding windows were sized to contain 20% of the total number of recorded time steps and shifted by a value of 1, corresponding to a 95% overlap. The relevant statistical measures within each window were recorded and visualized in a time sequence. Each timestamp corresponds to the starting time of the sliding window. The resulting spectrogram clearly shows the signal perturbation; as discussed in [7], the statistical features serve as various indicators of the SET behavior. The local maxima of γ (or κ) are used to define the total width of the event, whereas the peak in the μ is a direct estimate of the SET magnitude. Furthermore, the approximate rise time can be determined by finding the difference in the onset time of the event (the first peak in γ) and the time at which the peak μ occurs. In contrast, the fall time can be determined as the difference when the peak μ occurs and the second peak in γ. The σ^2 and σ features further serve as indicators of the transient time constants [7].

It is important to note that IRES spectrograms can be created from any signal metric (e.g., in Fig. 1, the cycle-to-mean phase jitter and instantaneous frequency) and any number of statistical measures. In this work, up to eight

statistical moment-generating functions are used. Then, the PLL's nominal behavior is compared to the behavior associated with SETs originating within the PLL subcircuits. Finally, ML is used to characterize events to identify the origin of the SETs within the device.

B. Device Under Test: A CMOS Phase-Locked Loop

The PLL used in this work has been discussed extensively in [6], [7], and [20]–[24] and consists of the phase-frequency detector (PFD), charge pump (CP), low-pass filter (LPF), voltage-controlled oscillator (VCO), and frequency dividers. The PLL was fabricated using a 130-nm CMOS technology available through the Metal Oxide Silicon Implementation System (MOSIS) Multi Project Wafer (MPW) service available through the University of Southern California's Information Sciences Institute. The VCO has a center frequency (frequency at which $V_{\text{inVCO}} = V_{\text{dd}}/2$) and a maximum frequency of approximately 200 and 530 MHz, respectively. The PLL's locking range is between approximately 40 and 350 MHz, over which the VCO is approximately linear with a gain of 7.75 GHz/V. In this article, SET data originating within the CP subcircuit are analyzed through IRES and the ML approach described herein.

III. Experimental Setup

SET data were obtained through TPA using high peak power femtosecond pulses at subbandgap optical wavelengths [25]–[29]. The TPA laser spot size had a diameter (full-length at half-maximum) of approximately 1.1 μm [28]. While various energies were used during irradiation, this work reports data at single energy to illustrate the technique's ability to discern spatial dependencies under constant charge deposition. It is important to note, however, that it is possible to use IRES to analyze transient variations due to differences in charge deposition and collection dynamics [7]. However, additional work is required to determine the feasibility of ML to discriminate such differences.

The device under test was mounted on a motorized xyz translation platform with 0.1 μm resolution, and the TPA laser was focused on the PLL's CP subcircuit, following an initial identification of the most vulnerable regions. The z-axis was fixed, and the xy position was manipulated to rasterize the laser across a 10 μm $\times$ 10 μm area of the CP subcircuit at a resolution of 0.2 μm. Waveforms were collected at the PLL circuit's output at the resulting ten thousand (10 000) strike locations, allowing for visualization of the 2-D spatial sensitivity. Ten independent measurements were taken at each strike location, amounting to 100 000 individual waveforms. Fig. 2 illustrates an example 2-D spatial map of the CP subcircuit regions sensitive to SETs [23]. The map was created by measuring the average of the maximum output phase displacements (i.e., the instantaneous cycle-to-cycle phase jitter) recorded from the ten measurements at each strike location.

Frequency and phase information contained in the PLL's output signal, as seen in Fig. 1, was used to create IRES spectrograms by discretely sampling the PLL output voltage and determining its instantaneous frequency at each clock

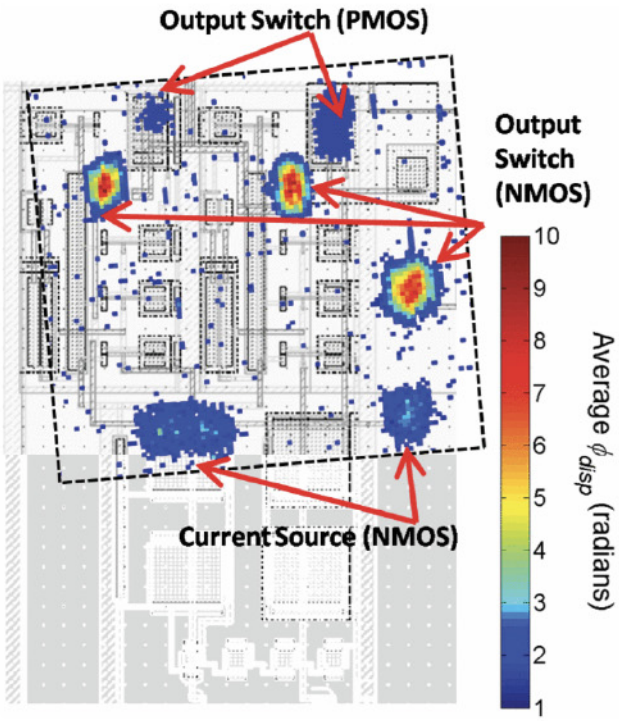

Fig. 2. Two-dimensional spatial map of the regions in the CP subcircuit sensitive to SETs. The experiment was performed using laser TPA at a step size of 0.2 μm. Each pixel represents the average maximum phase displacement (instantaneous cycle-to-cycle phase error) for ten SETs generated at each xy location. The image shows that the output of the CP circuit, in particular, the nMOS switches and current sources, contain the most sensitive junctions due to their ability to deplete the charge stored in the loop filter (after [23]).

edge. The instantaneous phase displacement of the signal was determined using cycle-to-mean (c2m) and cycle-to-cycle (c2c) phase jitter computations [23]. The root-mean-square (rms) of the phase jitter is often reported to quantify the spread in the phase spectrum and can be determined by finding the standard deviation of the c2c phase jitter. One common method for determining an SET's presence within the PLL's output is to threshold the instantaneous phase displacement at the rms phase jitter or some other arbitrary noise level. Furthermore, the maximum deviation and recovery times are generally the only metrics used for quantifying SETs. IRES retains all spectral content before, during, and after the transient.

Then, the frequency (f) and phase signals of interest are passed through a windowing function that calculates the waveform's statistical measures, such as γ, κ, σ^2, σ, and μ. Other moments may also be included. Here, we derive features using up to the eighth moment. The associated statistical values are vectorized and concatenated into a single IRES image. Note that this time-frequency analysis is analogous to the RF-DNA fingerprint generation process. An example output of this function is shown in Fig. 1, where γ, κ, σ^2, σ, and μ of a sample transients cycle-to-mean (c2m) phase jitter are illustrated along with the μ of the instantaneous frequency.

IV. kNNs Machine Learning

For this problem space, kNN [30] was chosen as the ML classifier for several reasons. First, kNN is computationally

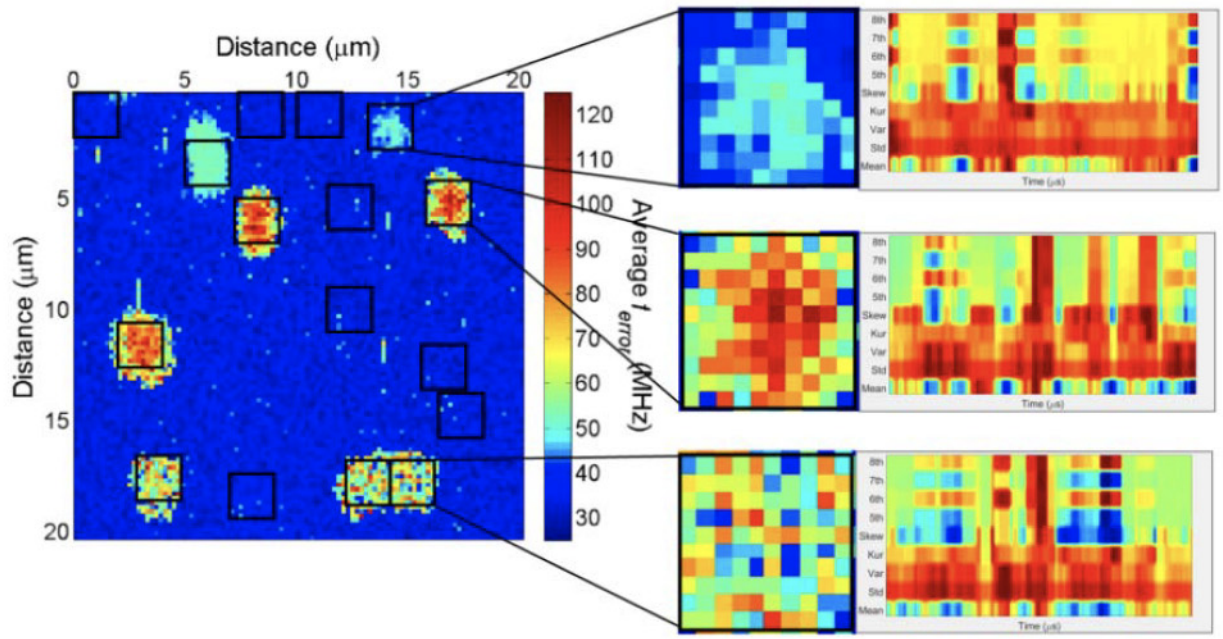

Fig. 3. Definition of the sample patches within the SET spatial maps. Also shown are aggregate IRES spectrograms from three patches. The spectrograms were generated by analyzing the PLL's output frequency, where the change in frequency correlates to the distinct aberration in the IRES image and includes eight statistical moments.

simple compared to complex algorithms like support vector machines (SVMs) [19] and has been successfully applied to the classification of handwritten digits, satellite images, and electrocardiogram (EKG) patterns [31]. Unlike SVM, which leverages kernel functions to map data points to higher dimensional feature spaces to achieve maximum class separation, *k*NN uses straightforward feature similarity measurements (e.g., Euclidian, Mahalanobis, Minkowski) to determine class assignment. Second, *k*NN eliminates the need for model fitting through a labeled training set of fingerprints to represent each of the known classes [31]. *k*NN, as a consensus-based classifier, assigns a to-be-classified IRES spectrogram as belonging to the class whose training data comprise the majority of the nearest neighbors [32]. Third, *k*NN may be readily deployed in SoC applications. There are on-chip architectures proposed for *k*NN [33] to allow for the IRES generation and *k*NN classification process to be performed locally. Finally, when *k*NN is updated with new data, it is done so in real-time without affecting accuracy, which implies that it could be leveraged to classify SETs of any origin, not just SETs within a PLL.

Fig. 3 illustrates an example of the spatial sensitivity of the CP subcircuit to SETs. The spatial map quantifies the average of the peak frequency deviation (f_{error}) obtained for the ten measurements. While the spatial map shows the average of the maximum f_{error} from the ten transient waveforms per pixel, the measurements were highly repeatable, with a maximum standard deviation of approximately 15%. The raw data are grouped in 3 μm $\times$ 3 μm patches as a known SET or as nominal behavior (noise). There are 16 patches total, eight patches for both groups, and 3200 waveforms within the patches. The event patches consist of two nMOS output switch patches, three pMOS output switch patches, and three nMOS current source patches. The *k*NN ML models were trained with independent measurements (from between one spatial map up to ten spatial maps) from the nominal patches and event patches. Individual models were created for c2m, c2c, and f signal metrics based on statistical data from up to eight moment-generating functions applied during the IRES sliding window analyses. The models were tested with samples from all patches. The highest priority goal was to accurately classify an event (identification/acceptance as an SET) versus nominal (rejection as an SET) and classify each event patch, thereby revealing the PLL's specific region that the event originated.

V. Statistical Feature Analysis

Classification results are presented in the form of error (confusion) matrices, as shown in Fig. 4. The error matrices show the number of measurements correctly predicted by the *k*NN models as either an SET (true positive or TP) or as a nominal/noise event (true negative or TN), as well as those incorrectly predicted by the *k*NN models as either an SET (false-positive or FP) or as a nominal/noise event (false-negative or FN). The positive predictive value (PPV) and negative predictive value (NPV), given by (1) and (2), are also displayed to indicate the overall ability of the model to predict the events as either SET events or noise (other)

$$\text{PPV} = \frac{\text{TP}}{\text{TP} + \text{FP}} \tag{1}$$

$$\text{NPV} = \frac{\text{TN}}{\text{TN} + \text{FN}}. \tag{2}$$

Signal Metric		Actual Class: SET	Actual Class: Noise	
Predicted Class	SET	TP	FP	*PPV*
	Noise	FN	TN	*NPV*

Fig. 4. Legend for the error (confusion) matrix to describe the classification of measurements as an SET or noise (non-SET) events. The number of samples reporting TP, FP, TN, and FN results from the kNN model are reported. The PPV and NPV are displayed to indicate the model's overall ability to predict the events as either SET events or noise.

c2c		Actual Class: SET	Actual Class: Noise	
Predicted Class	SET	1504	96	*94.0%*
	Noise	78	1522	*95.1%*

c2m		Actual Class: SET	Actual Class: Noise	
Predicted Class	SET	1571	29	*98.2%*
	Noise	36	1564	*97.8%*

f		Actual Class: SET	Actual Class: Noise	
Predicted Class	SET	1592	8	*99.5%*
	Noise	6	1594	*99.6%*

Fig. 5. Example classification results from the kNN model trained with data from nine out of ten spatial maps. A total of 3200 random samples from the tenth spatial map were selected and compared to known results. Results are provided for the kNN model trained with c2c, c2m, and f signal transformations and included features from eight statistical moment-generating functions.

A. Classification Accuracy Versus Signal Metric

Fig. 5 shows example classification results from the models trained with data from nine out of ten spatial maps. The 3200 samples from the patches within the tenth spatial map were selected and compared to the predicted results. Results are provided for the kNN models trained with either the c2c, c2m, or f signal transformation and features from eight statistical moment-generating functions. Greater than 94% classification (in terms of the PPV and NPV) is achievable when eight statistical moments and nine of ten sample sets are used to train the kNN model. When using the c2m and f signal metrics, the PPV and NPV exceeded approximately 98% with very few incorrectly classified results.

B. Classification Accuracy Versus Statistical Feature

Fig. 6 shows classification results in terms of the PPV and NPV based on the c2c, c2m, and f signal metrics. The various kNN models were trained from nine out of ten spatial maps, similar to the results shown in Fig. 5. In Fig. 6, results are provided from six models trained from either the first (mean or μ), second (standard deviation or σ and variance or σ^2), third (skewness or γ), fourth (kurtosis or κ), or all eight statistical moments obtained from the IRES analysis. Results indicate that the second moment appears to be the most informative statistical feature, resulting in PPV and NPV of over 95.4%. This result is consistent across all signal metrics evaluated, indicating that the rapid state transition at the SET onset is

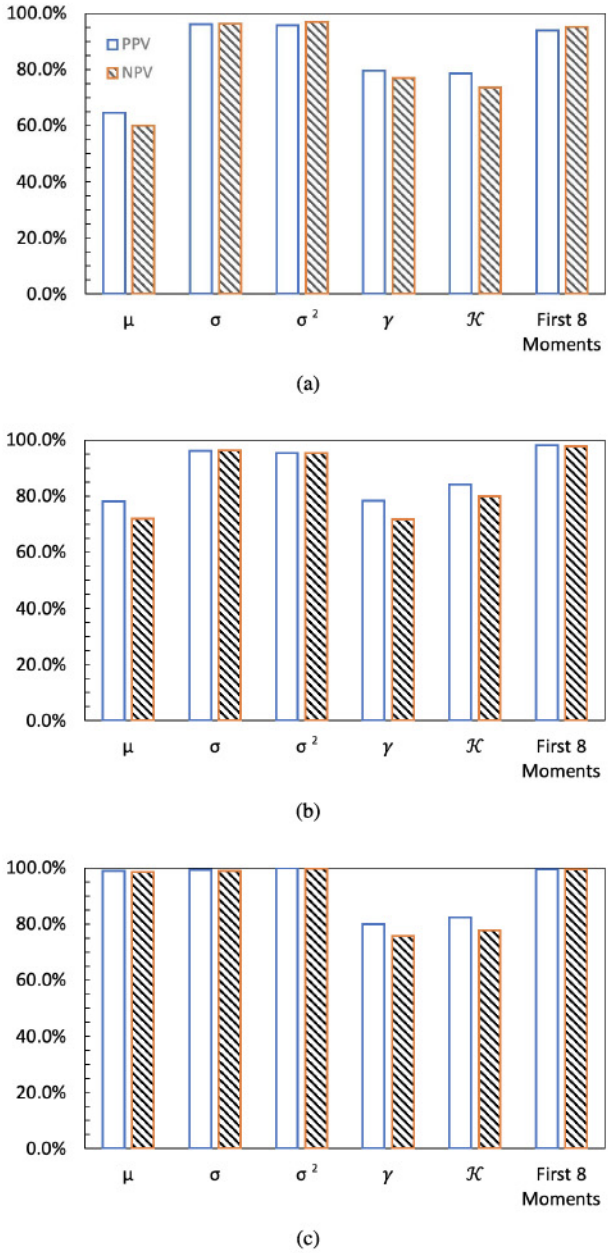

Fig. 6. PPV and NPV based on (a) c2c, (b) c2m, and (c) f signal metrics. The various kNN models were trained from nine out of ten spatial maps. The results of six models are presented. The models were trained from the first (mean or μ), second (standard deviation or σ and variance or σ^2), third (skewness or γ), fourth (kurtosis or κ), or first eight statistical moments obtained from the IRES analysis.

the most important defining feature (as captured by the IRES spectrograms). The inclusion of all eight statistical moments further improves the ability to detect the events, except the frequency signal metric, where a minor decrease was observed. In this case, the PPV and NPV are nearly 100% when using variance alone, and other low-performing moments tend to confuse the classifier.

C. Classification Accuracy Versus Number of Training Sets

The classification accuracy was evaluated as a function of the number of initial training sets. Fig. 7 shows the TP and

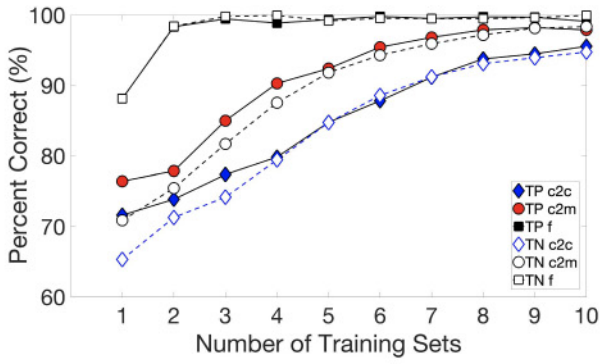

Fig. 7. SET classification accuracy showing the TP and TN values. Data are quantified as the percent correctly identified versus the number of sample sets used to train the kNN models for the c2c, c2m, and f signal transformations.

TN percentages (%) with respect to the number of training sets used to develop the kNN models. TP and TN percentages are shown in closed and open symbols, respectively, for each signal metric used to generate IRES spectrograms. Each model was trained with all eight statistical moments. The f signal transformation requires the least input data (two of ten sample sets) to achieve a greater than 98% for both correct acceptance and rejection. The c2m and c2c metrics require a significant increase in the training sets to achieve similar classification levels, requiring six and ten training sets, respectively, to achieve greater than 95% correct acceptance and rejection. It is also important to note that the deviation (displacement) in rms phase jitter (i.e., the second moment of the c2c phase jitter) and maximum frequency perturbation (i.e., the first moment of the instantaneous output frequency) are generally reported in the literature to describe the severity of SET in PLLs [6], [7], [20]–[24]. Results indicate that aside from the f signal metric, the c2m phase jitter is perhaps more informative for identifying SET phenomena compared to the c2c metric.

VI. Conclusion

This work employs IRES for the characterization of SETs in circuits and introduces the use of ML for the identification and analysis of SET phenomena. One-hundred thousand waveforms from a 130-nm CMOS phase-locked loop (PLL) were measured at the Naval Research Laboratory's TPA laser facility, and ML via a kNN algorithm was used to classify nominal data and SET data based on statistical features. The statistical features, derived from several standard circuit metrics and up to eight moment-generating functions, show that SETs can be automatically identified by the kNN models, with several features resulting in greater than 98% correct identification of SETs. The ability to design ML models to accurately classify the presence of radiation-induced transients through multiple signal metrics and statistical features suggests that it is possible to employ ML to aid in the automatic identification and discrimination of transient phenomena in multiple circuit families, including those in analog, digital, mixed-signal, and SoC applications. Furthermore, once an ML model is designed and trained with prior data, it may be possible for near real-time analysis of observed data, including *in situ* event detection and real-time classification of data.

References

[1] K. P. McCarty, J. R. Coss, D. K. Nichols, G. M. Swift, and K. A. LaBel, "Single event effects testing of the crystal CS5327 16-bit ADC," in *Proc. IEEE Radiat. Effects Data Workshop*, Jul. 1994, pp. 86–96.

[2] T. L. Turflinger, "Single-event effects in analog and mixed-signal integrated circuits," *IEEE Trans. Nucl. Sci.*, vol. 43, no. 2, pp. 594–602, Apr. 1996.

[3] N. J.-H. Roche, A. Khachatrian, J. H. Warner, S. P. Buchner, D. Mcmorrow, and D. A. Clymer, "Measurement and analysis of multiple output transient propagation in BJT analog circuits," *IEEE Trans. Nucl. Sci.*, vol. 63, no. 4, pp. 1986–1994, Aug. 2016.

[4] S. E. Armstrong, R. W. Blaine, W. T. Holman, and L. W. Massengill, "Single-event vulnerability of mixed-signal circuit interfaces," in *Proc. 12th Eur. Conf. Radiat. Effects Compon. Syst.*, Sep. 2011, pp. 485–488.

[5] M. Cabanas-Holmen, E. H. Cannon, T. Amort, J. Ballast, and R. Brees, "Estimating SEE error rates for complex SoCs with ASERT," *IEEE Trans. Nucl. Sci.*, vol. 62, no. 4, pp. 1568–1576, Aug. 2015.

[6] B. Patel *et al.*, "Ionizing radiation effects spectroscopy for analysis of total-ionizing dose degradation in RF circuits," *IEEE Trans. Nucl. Sci.*, vol. 66, no. 1, pp. 61–68, Jan. 2019.

[7] T. D. Loveless *et al.*, "Ionizing radiation effects spectroscopy for analysis of single-event transients," *IEEE Trans. Nucl. Sci.*, vol. 67, no. 1, pp. 99–107, Jan. 2020.

[8] D. R. Reising, M. A. Temple, and J. A. Jackson, "Authorized and rogue device discrimination using dimensionally reduced RF-DNA fingerprints," *IEEE Trans. Inf. Forensics Security*, vol. 10, no. 6, pp. 1180–1192, Jun. 2015.

[9] L. Xiao, L. Greenstein, N. Mandayam, and W. Trappe, "Fingerprints in the ether: Using the physical layer for wireless authentication," in *Proc. IEEE Int. Conf. Commun.*, Jun. 2007, pp. 4646–4651.

[10] B. Kroon, S. Bergin, I. O. Kennedy, and G. O'Mahony Zamora, "Steady state rf fingerprinting for identity verification: One class classifier versus customized ensemble," in *Artificial Intelligence and Cognitive Science*, L. Coyle and J. Freyne, Eds. Berlin, Germany: Springer, 2010, pp. 198–206.

[11] C. K. Dubendorfer, B. W. Ramsey, and M. A. Temple, "An RF-DNA verification process for ZigBee networks," in *Proc. IEEE Mil. Commun. Conf.*, Oct. 2012, pp. 1–6.

[12] D. R. Reising and M. A. Temple, "WiMAX mobile subscriber verification using Gabor-based RF-DNA fingerprints," in *Proc. IEEE Int. Conf. Commun. (ICC)*, Jun. 2012, pp. 1005–1010.

[13] D. R. Reising, "Exploitation of RF-DNA for device classification and verification using GRLVQI processing," Ph.D. dissertation, Dept. Elect. Comput. Eng., Air Force Inst. Technol., Wright-Patterson AFB, OH, USA, Dec. 2012.

[14] W. Wang, Z. Sun, S. Piao, B. Zhu, and K. Ren, "Wireless physical-layer identification: Modeling and validation," *IEEE Trans. Inf. Forensics Security*, vol. 11, no. 9, pp. 2091–2106, Sep. 2016.

[15] G. Baldini, R. Giuliani, and G. Steri, "Physical layer authentication and identification of wireless devices using the synchrosqueezing transform," *Appl. Sci.*, vol. 8, pp. 2167–2186, 2018.

[16] Q. Tian *et al.*, "New security mechanisms of high-reliability IoT communication based on radio frequency fingerprint," *IEEE Internet Things J.*, vol. 6, no. 5, pp. 7980–7987, Oct. 2019.

[17] F. Kandah, J. Cancelleri, D. Reising, A. Altarawneh, and A. Skjellum, "A hardware-software codesign approach to identity, trust, and resilience for IoT/CPS at scale," in *Proc. Int. Conf. Internet Things (iThings) IEEE Green Comput. Commun. (GreenCom) IEEE Cyber, Phys. Social Comput. (CPSCom) IEEE Smart Data (SmartData)*, Jul. 2019, pp. 1125–1134.

[18] G. Baldini, R. Giuliani, and C. Gentile, "An assessment of the impact of IQ imbalances on the physical layer authentication of IoT wireless devices," in *Proc. Global IoT Summit (GIoTS)*, Jun. 2019, pp. 1–6.

[19] D. Reising, J. Cancelleri, T. Daniel Loveless, F. Kandah, and A. Skjellum, "Pre-print: Radio identity verification-based IoT security using RF-DNA fingerprints and SVM," 2020, *arXiv:2005.09503*. [Online]. Available: http://arxiv.org/abs/2005.09503

[20] Y. Boulghassoul, L. W. Massengill, A. L. Sternberg, B. L. Bhuva, and W. T. Holman, "Towards SET mitigation in RF digital PLLs: From error characterization to radiation hardening considerations," *IEEE Trans. Nucl. Sci.*, vol. 53, no. 4, pp. 2047–2053, Aug. 2006.

[21] T. D. Loveless, L. W. Massengill, B. L. Bhuva, W. T. Holman, A. F. Witulski, and Y. Boulghassoul, "A Hardened-by-Design technique for RF digital phase-locked loops," *IEEE Trans. Nucl. Sci.*, vol. 53, no. 6, pp. 3432–3438, Dec. 2006.

[22] T. D. Loveless *et al.*, "A Single-Event-Hardened phase-locked loop fabricated in 130 nm CMOS," *IEEE Trans. Nucl. Sci.*, vol. 54, no. 6, pp. 2012–2020, Dec. 2007.

[23] T. D. Loveless, L. W. Massengill, W. T. Holman, B. L. Bhuva, D. Mcmorrow, and J. H. Warner, "A generalized linear model for single event transient propagation in phase-locked loops," *IEEE Trans. Nucl. Sci.*, vol. 57, no. 5, pp. 2933–2947, Oct. 2010.

[24] Z. Chen, M. Lin, Y. Zheng, Z. Wei, S. Huang, and S. Zou, "Single-event transient characterization of a radiation-tolerant charge-pump phase-locked loop fabricated in 130 nm PD-SOI technology," *IEEE Trans. Nucl. Sci.*, vol. 63, no. 4, pp. 2402–2408, Aug. 2016.

[25] D. Mcmorrow, W. T. Lotshaw, J. S. Melinger, S. Buchner, and R. L. Pease, "Subbandgap laser-induced single event effects: Carrier generation via two-photon absorption," *IEEE Trans. Nucl. Sci.*, vol. 49, no. 6, pp. 3002–3008, Dec. 2002.

[26] D. Mcmorrow *et al.*, "Three-dimensional mapping of single-event effects using two photon absorption," *IEEE Trans. Nucl. Sci.*, vol. 50, no. 6, pp. 2199–2207, Dec. 2003.

[27] E. W. Van Stryland *et al.*, "Two photon absorption, nonlinear refraction, and optical limiting in semiconductors," *Opt. Eng.*, vol. 24, no. 4, pp. 613–623, Aug. 1985.

[28] T. Boggess, K. Bohnert, K. Mansour, S. Moss, I. Boyd, and A. Smirl, "Simultaneous measurement of the two-photon coefficient and free-carrier cross section above the bandgap of crystalline silicon," *IEEE J. Quantum Electron.*, vol. 22, no. 2, pp. 360–368, Feb. 1986.

[29] A. Khachatrian, N. J.-H. Roche, D. Mcmorrow, J. H. Warner, S. P. Buchner, and J. S. Melinger, "A dosimetry methodology for two-photon absorption induced single-event effects measurements," *IEEE Trans. Nucl. Sci.*, vol. 61, no. 6, pp. 3416–3423, Dec. 2014.

[30] N. S. Altman, "An introduction to kernel and nearest-neighbor nonparametric regression," *Amer. Statistician*, vol. 46, no. 3, pp. 175–185, Aug. 1992.

[31] T. Hastie, R. Tibshirani, and J. Friedman, "The power spectral density," in *The Elements of Statistical Learning*. New York, NY, USA: Springer 2002, ch. 3.

[32] S. Theodoridis and K. Koutroumbas, *Pattern Recognition*. New York, NY, USA: Academic, 2003.

[33] M. Shoaran, B. A. Haghi, M. Taghavi, M. Farivar, and A. Emami-Neyestanak, "Energy-efficient classification for resource-constrained biomedical applications," *IEEE J. Emerg. Sel. Topics Circuits Syst.*, vol. 8, no. 4, pp. 693–707, Dec. 2018.